Die approbierte Originalversion dieser Diplom-/Masterarbeit ist in der Hauptbibliothek der Technischen Universität Wien aufgestellt und zugänglich.
http://www.ub.tuwien.ac.at

The approved original version of this diploma or master thesis is available at the main library of the Vienna University of Technology.
http://www.ub.tuwien.ac.at/eng

TECHNISCHE UNIVERSITÄT WIEN
Vienna University of Technology

Diploma Thesis

Carbon supersaturated solid solution coatings of refractory metals

carried out for the purpose of obtaining the degree of Dipl.-Ing. submitted at TU Wien, Faculty of Technical Chemistry, by

Barbara Osinger, BSc.

Mat.Nr.: 01326473

Schulgasse 82/7 1180 Wien, Austria

under the supervision of

Univ.Prof. Dipl.-Ing. Dr.mont. Paul Heinz Mayrhofer
Institute of Materials Science and Technology, E308

Vienna, April 2019

This work was supported by Prof. Ulf Jansson from the Ångström Laboratory, Uppsala University, Sweden

Affidavit

I declare in lieu of oath, that I wrote this thesis and performed the associated research myself, using only literature cited in this volume.

Date

Signature

Acknowledgements

First, I want to thank my supervisor Paul H. Mayrhofer for making this study possible in the framework of an Erasmus research stay in Uppsala, Sweden.

Furthermore, I am very grateful to Ulf Jansson for hosting me at Ångström Laboratory and for guiding me through my research in Uppsala. I want to express gratitude to my supervisor Stefan Fritze for providing me with the incredible opportunity and support to conduct this master thesis in the way I did. Thank you for your continuous help and guidance.
I want to thank Erik Lewin and Pedro Berastegui for all their technical support especially concerning Svanslös when it did not work properly.

I want to thank the whole thin film group and, in a broader sense, the whole department of Inorganic and Structural chemistry at Uppsala University for making me feel so very welcome in Sweden.

Last but not least, a special thanks to my family for their necessary support, and to my friends for their patience and never-ceasing encouragement along the way.

Table of contents

Abstract v
Kurzfassung vi
1. Introduction 1
2. Physical vapour deposition 5
3. Thin film growth 7
4. Structure zone model 8
5. Characterisation techniques 10
5.1. X-ray photoelectron spectroscopy (XPS) 10
5.2. Elastic recoil detection analysis (ERDA) 11
5.3. X-ray diffraction (XRD) 11
5.4. Nanoindentation 13
5.5. Scanning electron microscopy (SEM) 15
5.6. Transmission electron microscopy (TEM) 16
5.7. Atom probe tomography (APT) 16
6. Experimental setup 17
6.1. Magnetron Sputter Deposition 17
6.1.1. TaW(C) films 17
6.1.2. W(C) films 17
6.2. Annealing of the TaW(C) films 18
7. Results and discussion 19
7.1. Influence of the carbon concentration in W(C) thin film 19
7.2. Thermal stability of TaW(C) thin films 23
8. Conclusions 34
List of figures vii
List of tables ix
List of abbreviations x
List of references xii

Abstract

The vast demand for materials that can provide the challenging property combination of high hardness with ductility, as well as thermal stability and corrosion resistance, sparks extensive research including in the field of thin film technology. The addition of interstitial carbon to magnetron sputtered thin films poses an interesting approach to obtain coatings with superior mechanical properties, due to grain refinement hardening and solid solution strengthening. This study aims to investigate the limitations of the carbon supersaturation concept, in regard to possible industrial applications. Firstly, a variety of carbon concentrations in W(C) films was screened, to investigate the optimal compositional range, to begin with. Furthermore, the thermal stability of TaW(C) thin films with a particularly chosen composition was investigated.

For the magnetron sputtered W(C) films, the carbon concentration was varied in the range of 0 to 10 at.%. All films exhibited a single solid solution bcc structure, with the highest hardness of 31 GPa, at a reduced elastic modulus of 418 GPa, yielded for the film with the addition of 9 at.% of carbon. The TaW(C) films retained the solid solution bcc structure with a strong (110) texture even after vacuum annealing at 900 °C for 2 hours. No significant grain coarsening was observed, as the size of the grains remained consistent at around 20 ± 5 nm and no peak narrowing in the XRD patterns occurred. After annealing hardness increased significantly from 16.8 to 26.2 GPa, while the reduced E-modulus stayed constant at around 370 GPa.

Based on our results we can conclude, that the optimal concentration for carbon supersaturation in refractory metal thin films appears to be ranging from 8 to 10 at.%. Furthermore, no carbon precipitation occurred at elevated temperatures and the TaW(C) films even surpassed their already improved mechanical properties. With both superior mechanical properties and good thermal stability, the concept of carbon supersaturated multicomponent refractory metal coatings can be considered interesting for various potential applications.

Kurzfassung

Die große Nachfrage nach Materialien, welche die anspruchsvolle Eigenschaftskombination von hoher Härte mit Duktilität, sowie thermische Stabilität und Korrosionsbeständigkeit bieten können, motiviert umfangreiche Forschung speziell auch im Bereich der Dünnschichttechnik. Der Zusatz von interstitiellem Kohlenstoff in Magnetron gesputterten Dünnschichten, stellt eine interessante Herangehensweise dar, um verbesserte Eigenschaften durch Kornverfeinung und Mischkristallhärtung zu erzielen. Ziel dieser Studie ist es, die Grenzen des Konzepts der mit Kohlenstoff übersättigten Mischkristallschichten zu ermitteln. Zuerst wurde eine Vielzahl von Kohlenstoffkonzentrationen in W(C) Schichten getestet, um den optimalen Zusammensetzungsbereich zu ermitteln. Infolgedessen wurde die geeignete Zusammensetzung für die TaW(C) Schichten ausgewählt und deren thermische Stabilität untersucht.

Bei den Magnetron gesputterten W(C)-Schichten wurde die Kohlenstoffkonzentration im Bereich von 0 bis 10 at.% variiert. Alle Schichten wiesen eine krz Mischkristallstruktur auf, wobei die Schicht mit dem Zusatz von 9 at.% Kohlenstoff die höchste Härte mit 31 GPa und einem reduzierten E-Modul von 418 GPa ergab. Die TaW(C) Schichten wiesen selbst nach dem Vakuumglühen bei 900 ° C für 2 Stunden, eine krz Mischkristallstruktur mit einer starken (110) Texturierung auf. Keine nennenswerte Kornvergröberung konnte beobachtet werden, da die Korngröße konstant bei etwa 20 ± 5 nm blieb und es zu keiner Verringerung der Halbwertsbreite der Reflexe im Röntgendiffraktogramm kam. Nach dem Glühen erhöhte sich die Härte nochmal deutlich von 16.8 auf 26.2 GPa, während der reduzierte E-Modul konstant bei etwa 370 GPa blieb.

Aufgrund der Ergebnisse können wir zu dem Schluss kommen, dass die optimale Konzentration für mit Kohlenstoff übersättigte Refraktärmetallschichten im Bereich zwischen 8 und 10 at.% Kohlenstoff zu liegen. Darüber hinaus scheint bei erhöhten Temperaturen keine Kohlenstoffausscheidungen aufgetreten sind und sich die bereits optimierten mechanischen Eigenschaften der TaW(C) Schichten weiter verbesserten. Dank der verbesserten mechanischen Eigenschaften und einer guten thermischen Stabilität, könnte das Konzept der Kohlenstoffübersättigung von Refraktärmetallschichten, für verschiedene Anwendungsmöglichkeiten von Interesse sein.

1. Introduction

A major driving force for technical progress has always been, the incessant need for new materials with improved properties to meet the challenging and ever-changing demands of present-day applications. Nowadays scientists aim to develop materials with an improved and complex combination of properties, like high hardness and high wear resistance, as well as good thermal stability and corrosion resistance. At the same time, there is a strong push in the direction of weight reduction and cost-effectiveness. For certain applications, not even high-performance bulk materials can meet the requirements sufficiently anymore. This gave rise to a plethora of thin film techniques, including physical vapour deposition (PVD), as surface modification proved to be a pathway to enhance the physical and chemical properties of a tool, whilst maintaining relatively low material costs.

In 2004 the introduction of a new concept called high entropy alloys (HEAs) by Yeh et al. and multicomponent alloys (MCAs) by Cantor et al., posed a great leap forward in the field of alloy development [1,2]. High entropy alloys contain multiple principle alloy elements, usually five or more, in equimolar or near-equimolar ratios. More specifically the concentrations of each element should range between 5 to 35 at.% [3]. A different definition poses that a single phase solid solution has to be obtained [4]. And contrary to expectations, solid solution phases in either a bcc or fcc type structure, without any indication of any intermetallic phases, are observed. The explanation was, that for alloys with a greater number of constituent elements, the random solid solution is stabilized due to the increased configurational entropy ΔS_{mix} defined as:

$$\Delta S_{mix} = -R \sum c_i \, ln \, c_i \qquad (1)$$

where R is the general gas constant and c_i is the molar fraction of the element i. The entropy of the ideal solid solution should be larger than 1.61R, which is ΔS_{mix} for an equimolar alloy with five metals [3]. To describe HEAs another parameter, namely the enthalpy of mixing H_{mix} is commonly used. Given the total change of Gibbs free energy:

$$\Delta G_{mix} = \Delta H_{mix} - T\Delta S_{mix} \qquad (2)$$

If the mixing enthalpy H_{mix} is small compared to the $T\Delta S$ term, the formation of a solid solution may be energetically more favourable than intermetallic phases.

Recently, the incorporation of additional interstitial elements, like carbon, gave rise to a whole new set of HEAs with improved mechanical properties like increased hardness with unchanged ductility [5]. Based on the observation that p-elements in general, lead to grain refinement in magnetron sputtered films, which poses one approach to enhance the films mechanical properties. The grain refinement results from an enrichment on the surface of the grains during film growth, due to the limited solubility of the p-elements in bcc alloys. This repeatedly evokes nucleation of new grains and hence, a refined microstructure [6]. Carbon is especially interesting, as it is used as an alloying element in steel. Alloying with a small amount of interstitial carbon leads to a supersaturated solid solution, whereas high carbon concentrations would promote carbide formation. Doping HEAs with interstitial carbon could pave the way to increase yield and tensile strength at unchanged ductility. Li and Raabe mostly investigate FeMnCoCr based alloys. They have reported that carbon addition results in joint activation of twinning- and transformation induced plasticity [5]. They also found that doping with small amounts of boron, another p element, can lead to a 100% increase in yield strength and an increase in tensile strength by roughly 40% at comparable, or even better ductility [7]. However, concerning the stability at elevated temperatures and feasible compositional range, it is of great interest to investigate the limits of the supersaturation solid solution concept.

Most research is carried out in the field of bulk HEA materials, which are obtained by arc melting and casting methods. However, the concept can well be expanded to thin film technology in order to develop advanced protective coatings. Previous to the work of this study, CrNbTaTiW-C multicomponent films were deposited, with the addition of approximately 8 at.% of carbon, leading to the formation of a supersaturated solid solution. Both superior hardness and elevated crack resistance were observed for TaW-rich films compared to their near-equimolar counterparts [8]. This shows that the mechanical properties of HEAs can be tuned by changing the chemical composition, but the role of the different metallic alloy elements is unclear.

Recently, Fritze et al. have studied the ternary Ta-W-C system [9]. A quasi-binary system allows a more detailed study of the carbon influence on the metallic elements with the best mechanical properties in ref. [8] and avoids the complexity of the high entropy alloy. It was found that magnetron sputtered thin films of TaW with up to 6 at.% C could be deposited without carbide formation. X-ray diffraction (XRD) and atomic probe tomography (APT) of the films confirmed that an interstitial solid solution of C in the TaW alloys was obtained

without carbide formation. The Ta-W-C ternary phase diagram is shown in Figure 1, and the composition of the investigated films [9]is marked with a red dot. The very thin light blue strip in the TaW binary alloy region of the phase diagram marks the rather marginal maximum equilibrium solubility of carbon in the system. The carbon solubility in tantalum amounts to solely 0.7 at.% at 1000 °C and for tungsten, the solubility decreases down to only 0.05 at.% at around 2000 °C [10,11]. Consequently, the TaW-C films with the composition indicated in Figure 1, can be considered a highly supersaturated solid solution.

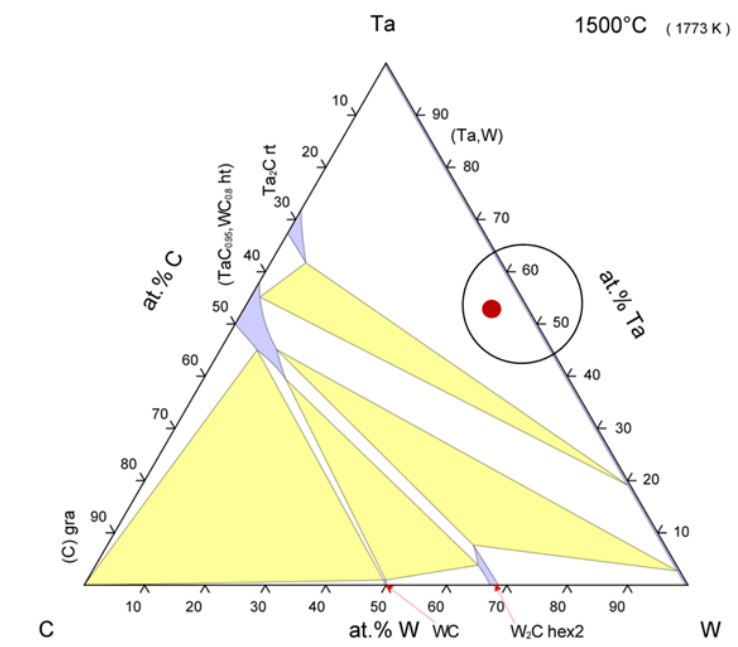

Figure 1: Ternary phase diagram of the W-Ta-C system [12]

The formation of such a supersaturated solid solution can be explained by the exceptional kinetics during PVD, for example very high quenching rates (>10^6 K/s) and other process related influences [13]. The extraordinarily high cooling rates for the vapour condensation lead to a quick energy loss and immobilization of the impinging atoms on the surface. This prevents the atoms from diffusing to the equilibrium phases with different chemical composition. Consequently, the formation of a single-phase solid solution is favoured, over film growth of a phase mixture given by thermodynamics. By definition, supersaturated solid solutions are thermodynamically not stable and could decompose into the equilibrium phases upon annealing. This would lead to altered film properties.

The aim of my master thesis is to investigate the stability of carbon supersaturated TaW alloys. In the first part of the thesis, W films were deposited with a varying amount of carbon, ranging from 0 to 10 at.%, to test the optimal carbon concentration and the limits of the supersaturation concept on a binary material system. For the second part, I have conducted an annealing study on magnetron sputtered TaW-C films, using the same approach as in ref. [14]. Two sets of near-equimolar thin films were investigated. One metallic TaW series as a reference and one supersaturated solid solution TaW(C) series, containing an additional 6 at.% of carbon. This carbon concentration was chosen as a middle ground, considering the results of the preliminary part of this study, ensuring both good mechanical properties and the definitive retention of a single-phase solid solution upon annealing. The effects of annealing on the supersaturated films were investigated with a wide range of analytical techniques such as X-ray diffraction, photoelectron spectroscopy, electron microscopy, and nanoindentation.

2. Physical vapour deposition

Thin film deposition techniques are separated into two major categories, called physical and chemical vapour deposition. The names of these techniques depend on the method used to create the vapour phase necessary for the deposition process. All films within the scope of this thesis were deposited by non-reactive magnetron sputtering, a classical physical vapour deposition (PVD) process.

PVD is an atomistic deposition process; therefore, the material is deposited atom-by-atom to form thin films. The resulting films can range from single crystalline to amorphous, from fully dense to loosely packed layers and from thin to thick. The film thickness usually ranges from a few atomic layers up to a few tenths of micrometres. However, thicker films (i.e. films that exceed the thickness of 1 micron) are generally referred to as coatings [15].

Generally, the PVD process can be described with three simple steps:

- Vapour generation of the layer-forming particles
- Transport of the gaseous phase to the substrate
- Condensation of the vapour on the substrate and consequently layer formation

Depending on the technique applied in the first step to generate the vapour phase, the PVD process can be further divided into two main categories: Evaporation, Sputtering. Ion Plating is a technique combining both Evaporation and Sputtering.

This thesis will solely focus on thin films synthesised by sputter deposition, more precisely DC magnetron sputtering, which presents the most commercially practiced method due to its simplicity and reliability. The methods main advantage is, that almost all elemental, alloy and compound materials can be sputtered, even high-melting-point refractory metals, whilst retaining the elemental composition of the bulk material [15]. In principle sputtering follows the physical model of momentum transfer via elastic collision, depicted schematically in Figure *2*. In the first step, a low-current high voltage glow discharge is generated. Therefore, the deposition chamber is firstly evacuated to minimize any background gases or contaminants. Then, an inert gas such as Argon is introduced into the chamber to reach a working gas pressure in the mTorr range. High voltages are applied between the cathode (target) and the anode

(substrate and chamber), which accelerates the primary electrons and leads to ionisation of the working gas. As a result, the emitted electrons can once again act as primary electrons, thus leading to a chain reaction, promoting further ionisation. However, only a small fraction of the gas, about 1 %, is ionised this way. The plasma contains an equal number of positive ions and negative electrons, whereby the ions are the species accelerated towards the negatively charged target. As a result, incident particles strike the surface and create a collision cascade, thus elastically transferring their energy to the target atoms. This causes a few of the atoms to be ejected into the vacuum environment, with enough kinetic energy to reach the substrate and condensate, forming a film [16].

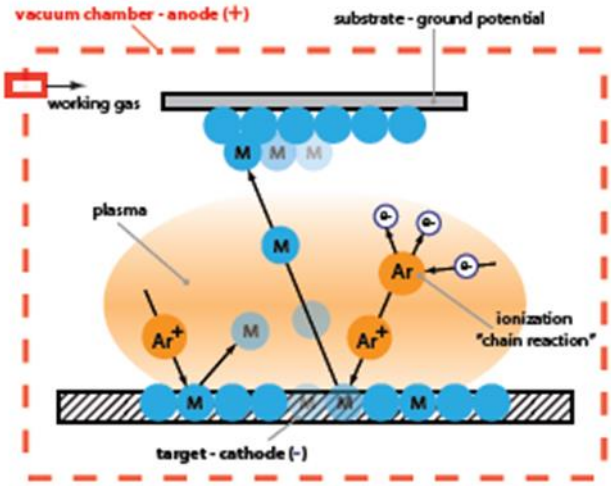

Figure 2: Schematic of a basic sputter process [17]

The efficiency of a deposition process, more precisely the removal of the target surface by ion bombardment, is described by the Sputter Yield S. It is defined as the number of sputtered target atoms per impinging ion. The higher the yield the higher the deposition rate. Many parameters influence the yield, such as the energy of the incident ions, the masses of ions and target atoms, the binding energies of the target surface atoms and the incident angle of the ions [18]. The process is on the other hand unaffected by the target temperature, given that the temperature, above which thermal evaporation occurs, is not surpassed. However, it should be noted that around 85 % of the incident ion energy is converted into heat, therefore adequate cooling of the target is indispensable to prevent damage to the target [19].

Sputtering with a direct current (DC) power supply is the basic and cheapest sputtering system. A glow discharge is initiated when a constant direct current potential of several kilovolts is applied between the positively charged chamber walls with the substrate and the negatively charged target. DC sputtering is limited to conductive materials, since sputtering of insulators, would lead to charging effects on the target surface. Thus, creating a barrier for arriving ions and consequently drastically decreasing the sputter yield or stopping the process altogether [20].

3. Thin film growth

The deposition conditions, such as chamber pressure, the substrate temperature and the bias voltage, have a significant influence on the film growth. The film formation can, however, be described by the following steps: In the first step of film growth the atoms from to gas phase condensate at the substrate surface. The adsorbed species, which are very mobile and evenly distributed, diffuse along the substrate surface to reach thermodynamically stable sites, where they coalesce into small clusters of subcritical size. In the next step, these clusters grow by further adsorbing impinging atoms and therefore surpass the critical cluster size. Consequently, competitive grain growth occurs, where sites with high diffusivity (low potential energy) overgrow ones with lower diffusivity (high potential energy) following the mechanism of Ostwald ripening. This decreases the island density drastically and nucleation on the substrate surface can occur once again [13].

Generally, three modes of film growth can be distinguished, based on various thermodynamic assumptions. Firstly, the Frank-van der Merwe or 2-dimensional growth, which is classified by a monolayer-by-monolayer growth, given the lattice parameter mismatch stays below a critical value [21]. Secondly, Volmer-Weber growth which assumes that crystalline films grow from 3-dimensional islands, arising from nuclei directly on the substrate surface [22]. And lastly, Stranski-Krastanov growth, which represents an intermediate mode, assuming island growth occurs, after a critical thickness of layer-by-layer morphology has been reached [23]. In Figure *3* a schematic view of three different thin film growth modes is depicted.

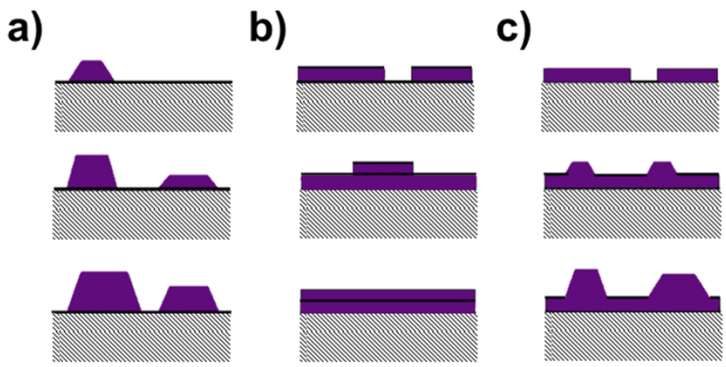

Figure 3: a) Volmer-Weber b) Frank van der Merwe and c) Stranski-Krastanov [24]

All three growth modes can be observed, implying that the theories complement each other. In essence, the growth mode can be predicted by thermodynamic considerations of the free energies of the three macroscopic surfaces – overlayer/vacuum, overlayer/substrate, and substrate/vacuum – interface [25]. In theory, the structure of the film is determined by the competition between the film-substrate interaction and the lateral interaction of ad-atoms within the film layer.

4. Structure zone model

The structure Zone Models (SZMs) are developed to link the structural evolution during film growth to the deposition parameters [26]. The first model was published in 1969 by Movchan and Demchishin. The diagram represented the microstructural evolution of several metallic coatings, obtained by evaporation, as a function of the homologous temperature, T_h (film growth temperature normalized by the melting point of the deposited material) [27]. The model consists of three zones, each with a characteristic structure and specific physical properties. The structures vary from highly porous, occurring in the low temperature and hence low ad-atom mobility regime of Zone I, to very dense with coarse grains in the high temperature and mobility Zone III [28]. 1973 Thornton further refined the SZM proposed by Movchan and Demchishin, by taking the deposition pressure and the substrate temperature into account. Along with Messier, who further added the energy of the ion bombardment, they introduced a new Zone T, which was believed to be a transitional regime between Zone I and II [16].

A schematic view of the SZM by Anders, which is most commonly used for modern PVD processes is shown in Figure 4. In this model, the generalized temperature T* and the normalized energy E* are used as the main axis. T* includes the homologous temperature and a temperature shift caused by the potential energy of arriving particles. E* replaces the linear pressure axis with a logarithmic axis to describe heating and displacement effects. The net film thickness t* on the z-axis provides information about the film thickness resulting from ion etching, sputtering and densification. This expansion of the SZM, allows for a proper description of structures obtained not only by evaporation but also by sputter and ion beam assisted deposition.

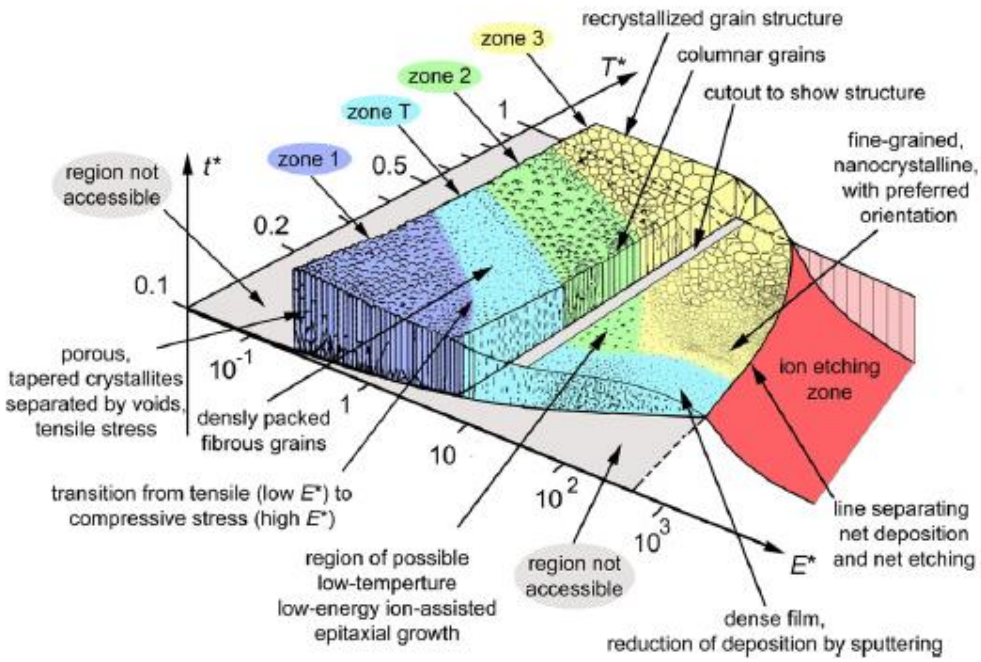

Figure 4: Structure Zone diagram by Anders [29]

5. Characterisation techniques

Methods to characterise thin film properties, like their microstructure and hardness, include Nanoindentation, X-ray diffraction (XRD) and various microscopic methods. The following chapter will give a short introduction to the theoretical background of the various techniques used in this study.

5.1. X-ray photoelectron spectroscopy (XPS)

X-ray photoelectron spectroscopy is an analysis method based on the photoelectric effect and often used for compositional analysis. Photoelectrons are generated when the material of interest is irradiated with x-rays. XPS is a highly surface sensitive technique since the mean free of electrons is relatively short in solids and therefore only information from the first few nm of the material can be obtained. Eq. (3) is used to calculate the electron binding energy (E_b), which is specific for each element and orbital, thus enabling elemental characterisation [30].

$$E_b = h\nu - E_k - \Phi \tag{3}$$

The kinetic energy of the photoelectrons (E_k) is acquired with the XPS measurement, $h\nu$ is the energy of the X-ray photons and Φ is the work function, which is a constant for the detector material. The binding energy is furthermore influenced by the chemical environment, which for example enables the estimation of free carbon in transition metal carbide materials.

The measurements of the films in this study were carried out on a Physical Electronics Quantera II system with monochromatic X-ray Al Kα radiation. Chemical information was obtained by the analysing the C1s as well as the W4f and Ta4f spectra. High-resolution spectra were acquired after the film surface was sputter-etched, to obtain the elemental information of the bulk without the interference of contaminants or oxide layers. The films were sputter-etched with 400 eV Ar^+-ions for 3 minutes, whereas the sputtered area was 1x1 mm^2.

5.2. Elastic recoil detection analysis (ERDA)

The elemental composition of surfaces and thin films is often determined by ion beam analysis techniques such as ERDA. The material of interest is bombarded with high-energy, high-mass projectiles which cause scattering and elastic recoil of the target's nuclei. The recoiling target atoms are measured to gain quantitative information on target composition [31]. The strength of ERDA is the good mass resolution (> 0.1 at. %) and sensitivity for light elements such as C, B, O, and N.

Iodine (36 MeV $^{127}I^{+8}$) atoms are used as projectiles that penetrate the film surface and eject the target atoms. The recoiled atoms are measured by a time of flight energy (ToF-E) detector. Two carbon-timing foils detect the time of flight of the recoiled atoms and a second detector measures the energy of the atoms. The atomic mass can be calculated by the following Eq. (4) [32].

$$E_i = \frac{M_i * v^2}{2} => \ M_i = \frac{2 * E * \Delta t^2}{L^2} \qquad (4)$$

Where Δt is the time of flight, L is the traveled distance, and E is the energy of the recoiled atoms. The composition was determined by Time-of-flight Energy ERDA (ToF-E-ERDA), carried out at the Tandem Laboratory at Uppsala University. As projectile species 36 MeV $^{127}I^{8+}$ ions were used and the base pressure in the experimental chamber was < 10^{-4} Pa.

5.3. X-ray diffraction (XRD)

X-ray diffraction analysis poses an especially powerful tool in the determination of structural information of crystalline matter, due to its fast and non-destructive nature. The principle of XRD is based on the diffraction of X-rays on the periodic structure of a crystalline material, whereby the scattered electromagnetic waves interfere both constructively and destructively. However, solely constructive interference of the diffracted X-rays can be detected and processed. The geometric condition for constructive inference is described by Eq (5):

$$n\lambda = 2\mathrm{d}\sin\Theta \qquad (5)$$

Where n is the order of diffraction, λ the wavelength of the incident beam (Cu Kα radiation with λ = 1.5406 Å was used in this study), d the lattice spacing and θ the angle of the diffracted beam [33]. The geometrical condition for constructive interference is shown schematically in Figure 5.

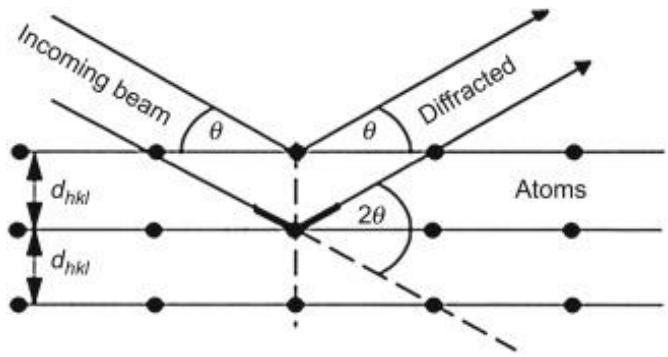

Figure 5: Bragg condition for diffraction on lattice planes [34]

Based on the recorded diffraction pattern micro- and macrostructural information such as crystal structure and lattice parameters can be deduced. qualitative phase analysis can be investigated. The peak intensity can provide further such as texture. The peak width can be correlated to crystallite size, compositional heterogeneity within the analysed crystallite (leading to a distribution of the lattice parameter), as well as the occurrence of strain [35].

Within this work, two different set-ups were used. The angle of the incoming X-rays (θ) and the angle of the detected outgoing X-rays (θ) are the same in the Bragg-Brentano geometry. This method is therefore often called θ2θ scan. For this kind of set-up, only the X-ray waves scattering on the crystal planes parallel to the surface are detected. The diffraction occurring with the Bragg Brentano geometry is shown schematically in Figure 6. Apart from the phase composition, additional information about the preferential grain orientation, with respect to the substrate surface, can be obtained [36].

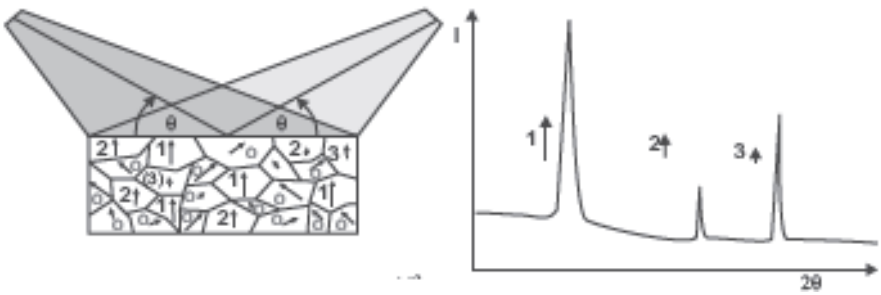

Figure 6: Bragg-Brentano diffraction [34]

The second set-up is the grazing incidence X-ray diffraction (GIXRD), shown in Figure 7(a) which was developed for the analysis of thin films. For this geometry, the incident X-ray beam is held at a constant small angle of incidence and only the detector is moved over a 2θ range. Contrary to the Bragg Brentano geometry, the scattering vector is no longer perpendicular to the sample surface but instead is changing throughout the measurement. Therefore, all lattice planes, not just the ones parallel to the sample surface, contribute to the diffraction pattern. Another advantage is the increased diffraction intensity of the thin film because the X-ray beam travels a longer path within the film [37,38]. The dependence of the probe volume on the incoming angle θ is shown in Figure *7*(b).

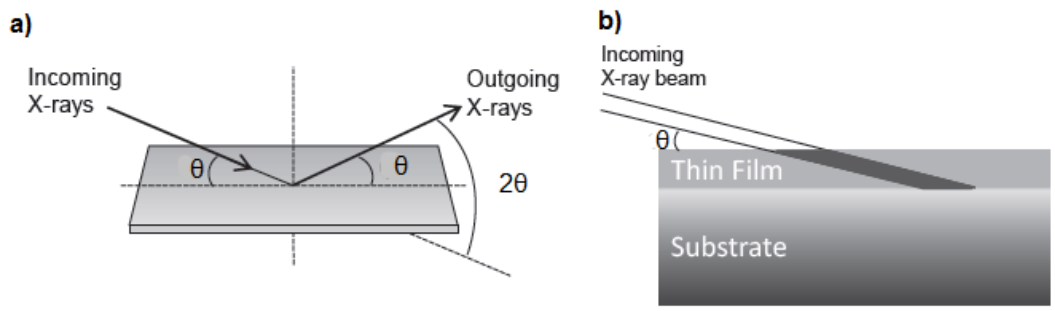

Figure 7: a) XRD geometry b) dependency of the diffraction volume with the incoming angle θ [39]

The measurements in this thesis were performed on a Siemens D5000 for the GIXRD and a Bruker D8 advance diffractometer for the θ2θ-XRD, using Cu Kα radiation. The $K\alpha_2$ signal in the θ2θ measurements was cancelled out by a monochromator. The lattice parameters were determined using the observed (110) and (200) peaks assuming a body-centred cubic structure.

5.4. Nanoindentation

Hardness is defined as the resistance of a material to plastic deformation when a localized compressive force is applied. Nanoindentation proves to be the method of choice to quantify the hardness of thin films, as the penetration depth of conventional hardness measurement methods would exceed the thin film thickness. During the measurement, the indenter, a diamond tip of various shapes and sizes, is forced into the material under controlled loading conditions. The penetration depth usually ranges within the nm to μm scale. As a rule of thumb, the penetration depth should stay within 1/10 of the film thickness, to minimise the influence of the substrate material.

Information about the hardness and elastic modulus of a material is deduced from the load-displacement curve, recorded during one loading/unloading cycle, according to Oliver and Pharr [40]. In Figure 8 a typical load-displacement curve is shown where h_{max} corresponds to the maximum penetration depth, h_r to the residual penetration depth, h_e to the elastic penetration depth, h_c to the depth of the contact circle, P_{max} to the maximal load, and dP/dh to the initial unloading stiffness [41].

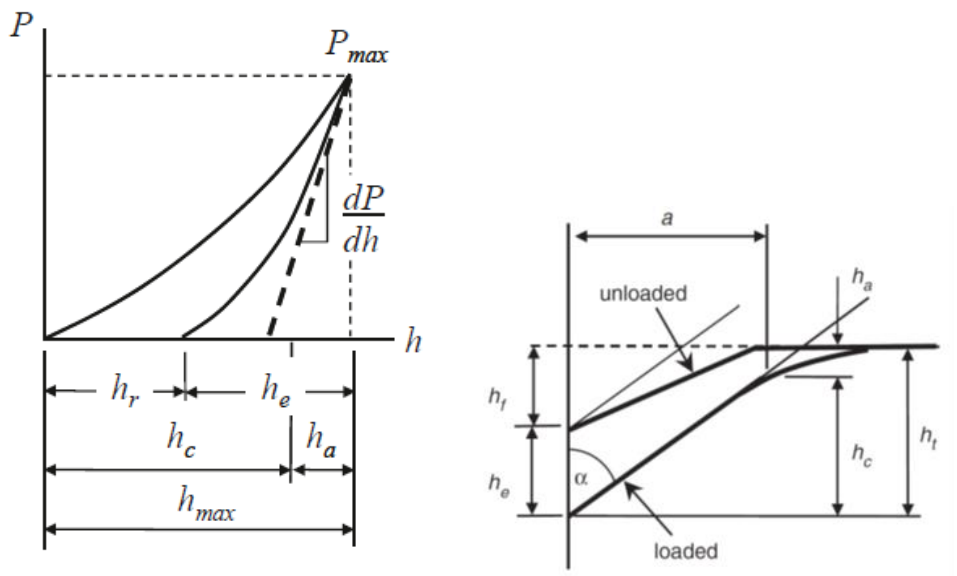

Figure 8: Load-displacement curve [41,42]

The hardness of a material is equal to the ration of applied load P_{max} to the area of contact A (projected area of contact at the maximum load), as shown in the Equ. (6). Given the Poisson ratio and indentation modulus of the indenter, the reduced elastic modulus E_r of the measured material can be calculated according to Equ. (7) [40]:

$$H = \frac{P_{max}}{A} \tag{6}$$

$$\frac{1}{E_{eff}} = \frac{(1-\upsilon^2)}{E} + \frac{(1-\upsilon_i^2)}{E_i} \tag{7}$$

The hardness of the deposited coatings was measured using a CSM Instruments Ultra Nano Hardness Tester (UNHT) equipped with a diamond Berkovich tip. Load-displacement curves were acquired at 20 different spots on the film surface in sinus mode with an amplitude of

0.25 mN and a frequency of 5 Hz. The maximum indentation load was set to 6 mN/min and the loading and unloading rate to 2.5 mN/min. Average values of at least 15 indents were used.

5.5. Scanning electron microscopy (SEM)

The most common imaging method in thin film technology is scanning electron microscopy (SEM), where a focused electron beam is used, which provides a higher spatial resolution than optical microscopy using visible light. Cross-sectional measurements are performed to gain information about the layer thickness. The top-view measurement can provide an insight into both the surface roughness and the grain size, or more precisely the column width of the film. Furthermore, an energy dispersive x-ray spectroscopy (EDS) detector is mounted to the SEM and can provide additional information about the composition of the sample [43].

Upon interaction of the primary electron beam with the sample, elastic and inelastic scattering occurs. Consequently, signals from various depths within the so-called interaction volume, are produced, as shown schematically in Figure 9. Secondary (SE) and Auger electrons are emitted close from the sample surface. Hence, they provide high-resolution images of the surface topography. Backscattered electrons (BSE) are emitted from deeper within the interaction volume and result from the elastic scattering of the primary electrons. Additionally, the emitted characteristic x-rays can be measured via EDS to identify the elemental composition [44].
A Zeiss Merlin SEM microscope, with an in-lens detector and a 5 keV acceleration voltage, was used to investigate the surface morphologies of the films deposited on Al_2O_3 substrates.

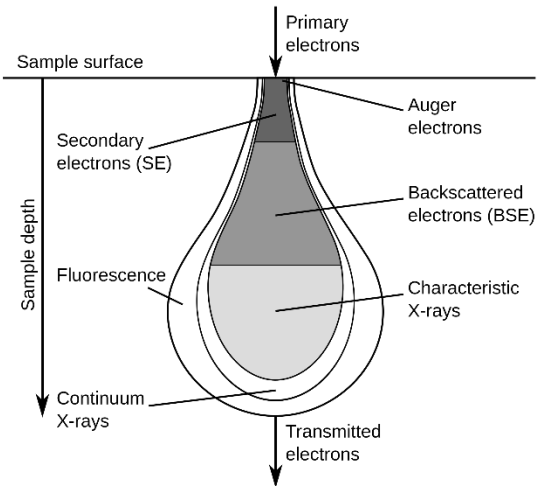

Figure 9: Pear-shaped interaction volume

5.6. Transmission electron microscopy (TEM)

Transmission electron microscopy (TEM) is a technique that allows imaging with atomic resolution. Scanning transmission electron microscopy (STEM) is a setup in TEM where a highly focused electron probe is used to scan across the sample to collect data [45]. All images within the framework of this thesis were acquired in STEM mode. Furthermore, an energy dispersive spectrometer was used for elemental mapping. The TEM measurements were carries out with 200 kV acceleration voltage on a probe corrected FEI Titan Themis instrument equipped with the SuperX EDS system.

5.7. Atom probe tomography (APT)

Atom Probe analysis poses an important analytical tool for atomic imaging combined with elemental analysis of atomic layers. Pulsed-field evaporation is used to extract the chosen surface atom and pass it through a hole into the commonly used time of flight (TOF) mass spectrometer. This allowed the measurement of “in-depth” compositional maps. A three - dimensional reconstruction of a sample composition can be obtained either by moving the sample relative to the probe hole to scan the specimen surface or by using a two - dimensional detector to analyse the ions emitted from the surface [46,47]. The corresponding technique of 3D-AP is also referred to as atom probe tomography (APT), in analogy to conventional tomography, which produces 3-D images from consecutive slices [48].

6. Experimental setup

6.1. Magnetron Sputter Deposition

6.1.1. TaW(C) films

All thin films were synthesized using a UHV DC magnetron sputtering deposition system equipped with four magnetrons. The chamber was evacuated to a base pressure below 10^{-8} Pa. The thin films were deposited by non-reactive DC-magnetron sputtering employing the two-inch circular targets: segmented Ta/W (1:1) and a C target. The two-inch targets were mounted in a sputter down configuration and tilted towards the centre of the substrate holder. All targets had a claimed purity of 99.9%. The substrate holder was rotating during the deposition in order to enhance the film homogeneity. Si (001) and α-Al_2O_3 (001) substrates were used. Prior to film growth, the substrates were heated to 300 °C for at least 1 h to minimise the risk of temperature gradients. An Ar^+ plasma was ignited at 0.6 Pa, using a 42 sccm Ar gas flow rate and a DC bias voltage of −100 V was applied to the substrate table during all depositions. The current on the Ta/W target was held constant while the current on the C target was either 0 or 40 mA. In order to simplify the cross view SEM, (001) silicon wafers with a thickness of 0.5 mm were used, while the 0.5 mm thick Al_2O_3 substrates were used for the XRD, XPS, top-view SEM, TEM and hardness measurements [8].

6.1.2. W(C) films

The W(C) films were synthesized using a different UHV DC magnetron sputtering deposition system equipped with four magnetrons. The base pressure in the system was below 10^{-7} Pa. The thin films were deposited by non-reactive DC-magnetron sputtering employing two three-inch circular targets: a W and a C target. All targets had a claimed purity of 99.9%. The substrate holder was rotating during the deposition in order to enhance the film homogeneity. The films were deposited on Si (001) and α-Al_2O_3 (001) substrates. Prior to film growth, the substrates were heated to 300 °C for at least 1 h to minimise the risk of temperature gradients. An Ar^+ plasma was ignited at 0.6 Pa, using a 60 sccm Ar gas flow rate and a DC bias voltage of −150 V was applied to the substrate table during all depositions. The current on the W target was constant at 800 mA at 195 V while the current on the C target was varied from 110 to 180 mA

with 370-400 V. The sputter process was carried out for around 6 hours, to yield films within the range of 3-5 µm. For the XRD, XPS, top-view SEM and hardness measurements 1 mm thick Al_2O_3 substrates were used.

6.2. Annealing of the TaW(C) films

For the investigation of their thermal stability, the as-deposited samples were annealed at 500 and 900 °C for 2 hours. Coatings on α-Al_2O_3 Substrates were used to avoid the formation of silicides. The samples were placed in a UHV furnace within an α-Al_2O_3 crucible. The furnace was repeatedly flushed with Ar and eventually evacuated to a pressure below $2 \cdot 10^{-6}$ Pa. The specimens were kept at RT for three and a half hours to reach a stable vacuum. The samples were then heated to 50 °C and kept at this temperature for 30 min to remove any organic remnants on the sample surface. The specimens were further heated to the target temperature of 500 or 900 °C respectively and kept there for 2 hours before being let to cool down. The annealing step is compactly summarised in Table 1.

Table 1: Heating profile of the annealing step

Temperature (°C)	Heating rate (K/min.)	Dwell time (h)
RT	-	3,5
50	2	0,5
500/900	5	2

7. Results and discussion

Within the scope of this study, both TaW and pure W films with the addition of small amounts of carbon were investigated. A variation of carbon concentrations was tested for the system W-C to investigate the maximum supersaturation limits of the solid solution structure. A suitable composition was determined and implemented on the more complex ternary system Ta-W-C. Furthermore, the thermal stability of the TaW(C) films was studied, in consideration of possible applicability.

7.1. Influence of the carbon concentration in W(C) thin film

For the first part of this study, W films with a varying amount of carbon were deposited. The aim of this study was to investigate the maximum solid solubility in pure W and the influence of C content on the mechanical properties. XPS proved to be an unsuitable method to analyse the C content in W films since there is an overlap between the C1s peak and shake-ups of the W4d peaks. The compositions of the films were therefore determined with ERDA and shown in Table 2.

Table 2: Chemical composition of the W(C) samples from ERDA

Sample	W [at.%]	C [at.%]
W(C)0	100	-
W(C)5	95	5
W(C)6	94	6
W(C)9	91	9
W(C)10	90	10

The θ2θ-diffraction patterns of the W(C) are presented in Figure 10. The diffraction patterns only show (hh0) peaks from a cubic A2 (bcc, $Im\bar{3}m$) phase with a <110> preferred orientation. A slight shift of the peaks towards lower angles as a function of the carbon content could be detected. The cell parameter was determined by evaluating the position of the (110) peak in the θ2θ-XRD patterns. The cell parameter for the pure W film is in agreement with values obtained for bulk α-W of a=3.165 Å [49]. An increase as a function of carbon content, reaching a maximum value of a=3.184 Å at 10 at.% carbon, was observed.

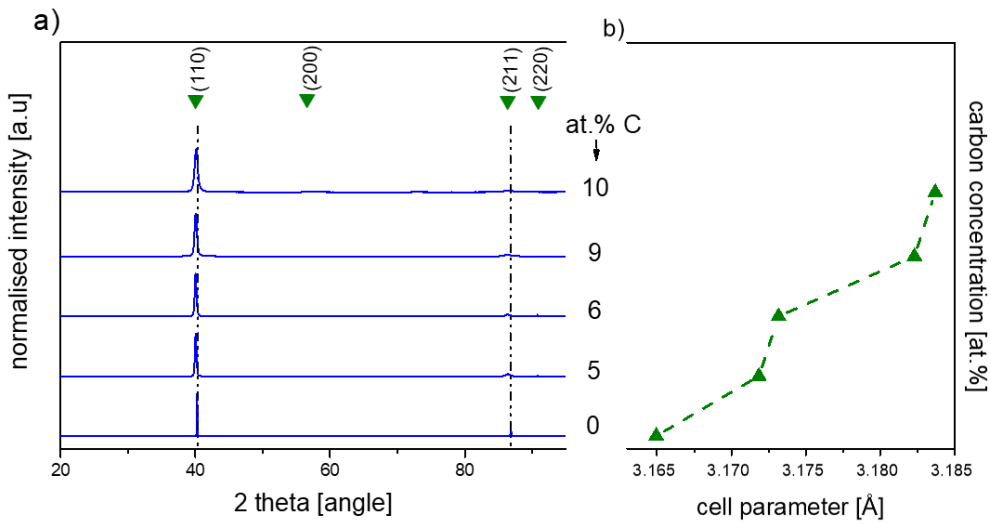

Figure 10: (a) θ2θ -XRD patterns of the W(C) films with varying carbon concentrations. The green triangles and dashed lines indicate the peaks of the bcc phase. (b) Their respective cell parameters.

The expansion of the unit cell is a consequence of the dissolved carbon in the solid solution structure. The solubility of 10 at.% C into bcc-W is much higher than predicted by thermodynamics (see Figure 1). This can be explained by the exceptional kinetics during the PVD process. Extremely high cooling rates for the vapour condensation lead to an immense energy loss, leaving the impinging atoms immobilized on the surface at non-equilibrium sites. A significant amount of energy would be necessary for the atoms to reshuffle in order to grow in three separate phases. Consequently, the formation of a single-phase solid solution is favoured, over film growth of a phase mixture given by thermodynamics. Furthermore, supersaturated solid solutions of C have been observed also in other studies. For example, Palmquist et al. determined a lattice expansion of 2% at 7at.% C [50]. Pauleau et al found a lattice dilatation of 2% at around 10 at.% C determined by the shift of the (110) peak [51]. An increase of the carbon content led to an increase of the FWHM of the (110) peak and therefore follows the same trends as the TaW(C) series and the results published by Fritze et al. [8].

In Figure 11 the GI-XRD patterns are plotted as a function of the carbon concentration. No peaks of additional phases were found in the diffraction patterns, indicating that a single solid solution structure was obtained for all carbon concentrations.

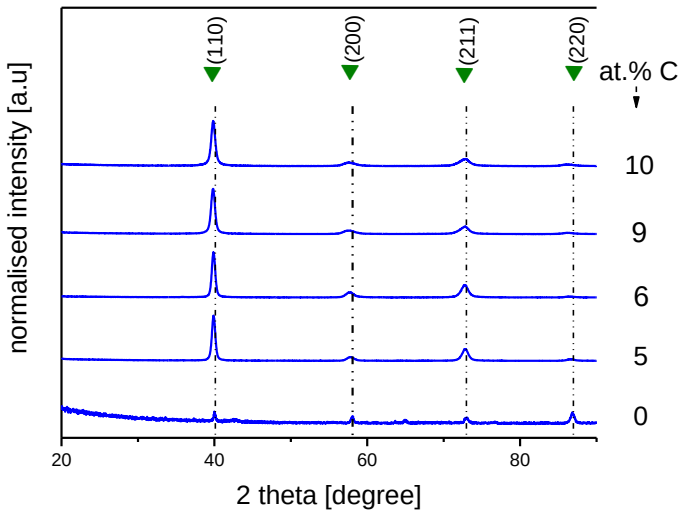

Figure 11: GI-XRD patterns of the W(C) films with varying carbon concentrations

The top-view SEM images in Figure 12(a-d) display the surface morphologies of pure W and W(C) films. The pure W film exhibits a smooth surface morphology with an angular orientation relationship. The grains also appear the have a lamellar-like shape. The grains are 25 ± 5 nm in width and 200 ± 20 nm in length. The morphology of the W(C) film with 6 at.%, exemplarily shown in Figure 12(c) and (d), is characteristic for all films containing carbon. The morphology appears more slap like, with the slap like grains overgrowing each other. The grains appear to be more refined compared to the metallic counterpart, with a column width of about 15 ± 5 nm. The orientation of the grains for the carbon-containing films is more random than the metallic counterpart. This change in morphology is attributed to the carbon which enriches on the surface of the growing grains and leads to renucleation, resulting in a more polycrystalline microstructure.

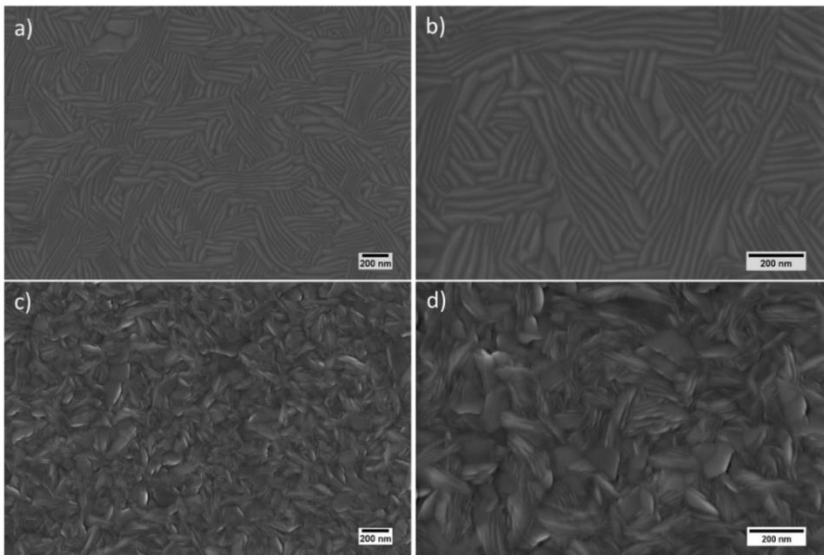

Figure 12: SEM top view of a) and b) pure W, c) and d) W(C) with 6 at.% of carbon

In Figure 13 both the hardness H and the reduced elastic modulus E_r of films with a varying carbon concentration are shown. The addition of carbon led to a significant increase in hardness H, from 15 GPa for the pure W film, to values above 31 GPa. The hardness appeared to peak around 9 at.% of C with 31 GPa, decreasing with the further addition of carbon. It is also noteworthy that the decrease is not very significant and well within the range of error. The high hardness for metallic bcc films is in excellent agreement with the results of Palmquist et al. which state a hardness of 13-25 GPa, depending on the substrate material used and hence the crystallinity [50]. The elastic modulus displayed an opposing trend, decreasing from 452 GPa for pure tungsten to a minimum of 418 GPa for the film containing 9 at.% of C.

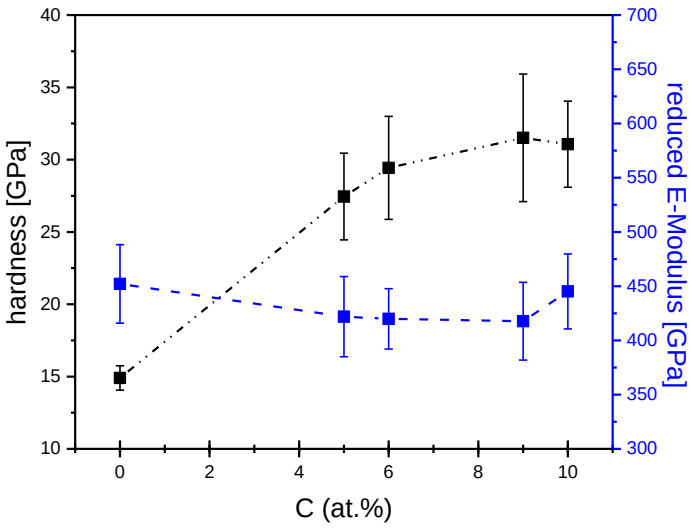

Figure 13: Hardness H and reduced elastic modulus Er of the W(C) films as a function of the carbon concentration

The films ranging around 6-10 at.% of carbon exhibit similar hardness and elastic modulus values. The superior mechanical properties are presumably due to a refined microstructure and a higher degree of polycrystallinity, caused by the carbon during grain growth. Grain refinement is a desirable hardening mechanism because it strengthens the material without a trade-off concerning toughness.

7.2. Thermal stability of TaW(C) thin films

For the second part of this study, the thermal stability of TaW(C) films was studied. The results in Figure 13 suggested that a C content ranging between 8-10 at.% yields the best mechanical properties. However, with C concentrations this high, carbides are more likely to form upon annealing. Therefore, I have chosen to study TaW films with a C content of about 6 at% considering that W(C) films with 6 at% of C exhibit roughly the same hardness and E-modulus as 10 at% but with a lower risk of carbides forming. Two series of near-equimolar films of TaW, one with and one without the addition of carbon, were deposited. The magnetron settings of the metal targets were kept constant to ensure the same relative concentration of tantalum and tungsten in all films. The chemical composition was determined by APT and TEM EDS and is shown in Table 3.

Table 3: Chemical composition of the TaW(C) samples from APT [9] and TEM EDS

Sample	Metal content [at.%]		C [at.%]
	Ta	W	
TaW	55	45	-
TaW(C)	51	43	6

The θ2θ-diffraction patterns of the TaW in Figure 14 and TaW(C) in Figure 15 only show (hh0) peaks from a cubic A2 (bcc, $Im\bar{3}m$) phase with a <110> preferred orientation. The reflection at 2θ =41.68° clearly visible in Figure 15(a), corresponds to the (006) peak of the sapphire substrate. No peaks of additional phases were found in the diffraction patterns.

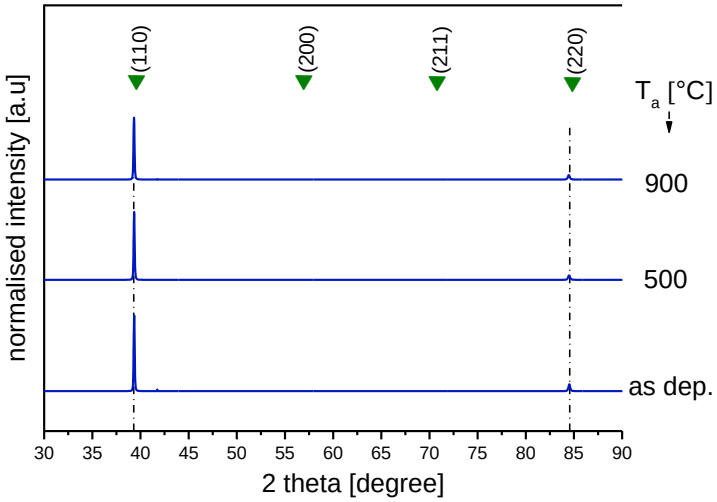

Figure 14: θ2θ-XRD patterns of the TaW films in the as-deposited state and after annealing at 500 °C and 900 °C. The green triangles and dashed lines indicate the peaks of the bcc phase.

The cell parameter of the as-deposited TaW films was a=3.24 Å. Annealing at 900 °C led to a reduction of the cell parameter to a=3.23 Å. In contrast, the cell parameter of the TaW(C) films decrease as a function of the annealing temperature from around a=3.28 to a=3.24 Å, which corresponds to the cell parameter of the pure TaW films before annealing. The reduction of the unit cell parameter could be either caused by a relaxation of the structure, or by depletion or reshuffling of carbon in the structure.

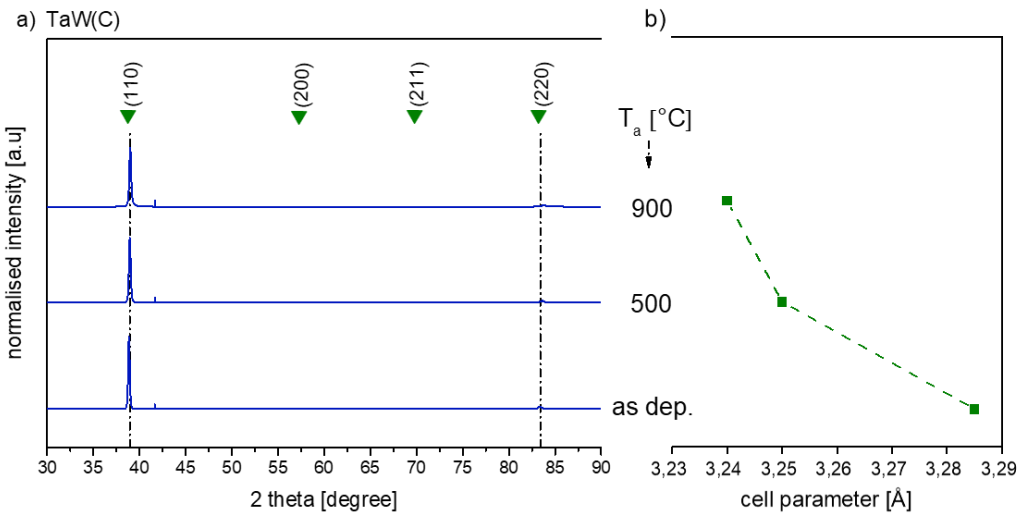

Figure 15: a) θ2θ-XRD patterns of the TaW(C) films in the as-deposited state and after annealing at 500 °C and 900 °C and b) their respective cell parameters.

In Figure 16 the GI-XRD diffraction patterns the as-deposited annealed and the state, but also the metallic TaW and the TaW(C) films are compared with each other. The GIXRD diffraction patterns confirm the presence of the cubic A2 phase, as observed for the θ2θ-XRD patterns.

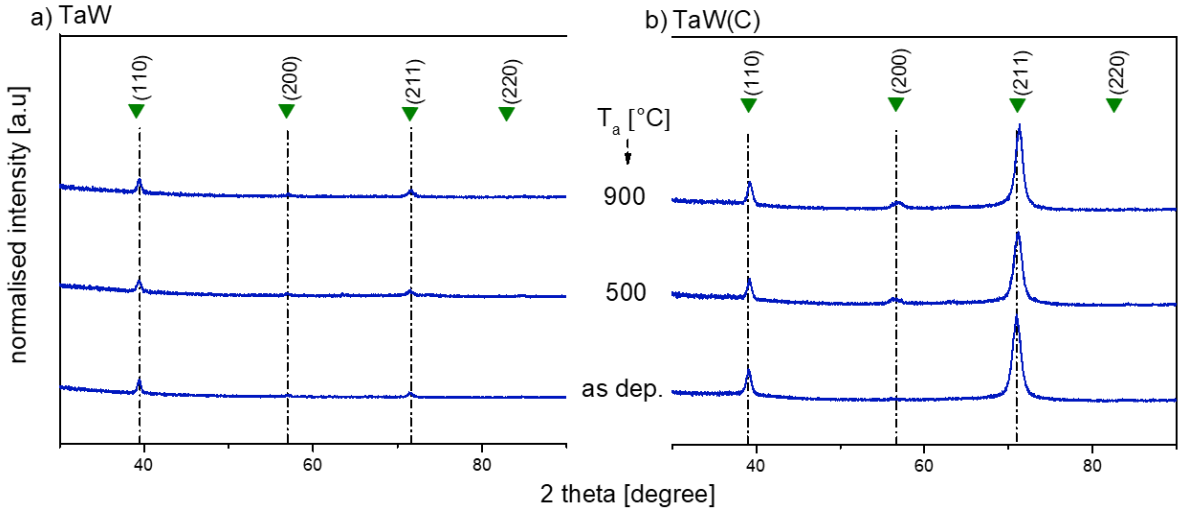

Figure 16: GIXRD patterns of a) TaW films and b) TaW(C) films as-deposited, annealed at 500 °C and 900 °C. The green triangles indicate the peaks of the bcc phase.

No indications of carbide formation or precipitation of carbon were observed in the GIXRD patterns. Furthermore, no significant decrease in the FWHM of the peaks could be observed, indicating that grain coarsening was suppressed during the thermal treatment. However, a slight shift of the peak positions towards higher angles as a function of the annealing temperature could be detected. This is especially conspicuous for the (211) peak of the TaW(C) samples in Figure 16(b). The decrease of lattice parameter is in agreement with the observation made for the θ2θ XRD patterns.

The High-resolution XPS spectra of the TaW(C) series are shown in Figure 17. The C1s spectra exhibit two peaks at around 282.5 and 284.5 eV, which are attributed to the carbidic Me-C (carbon in a metal environment) and the C-C (carbon in a carbon environment) free carbon, respectively. However, no further distinction between Ta-C and W-C, or the hybridisation of the free carbon was made for the peak fitting.

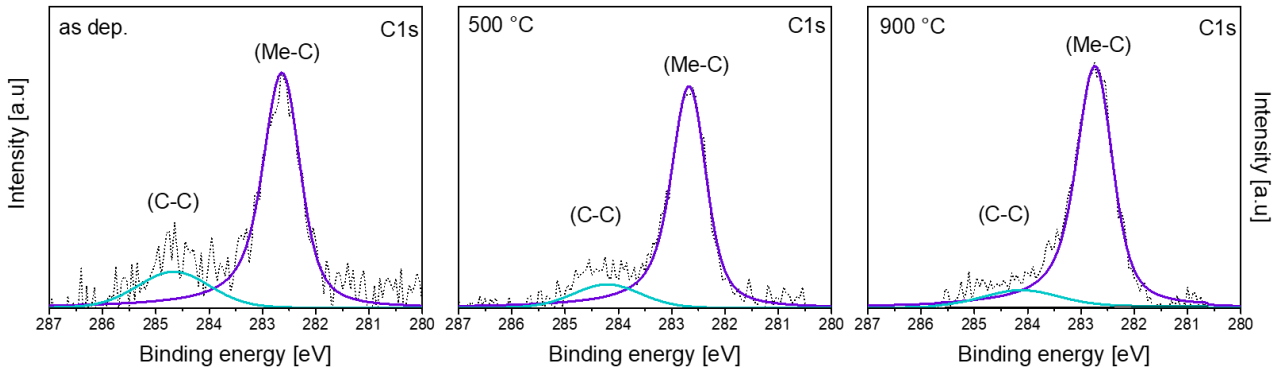

Figure 17: XPS C1s spectra of TaW(C) as-deposited, annealed at 500 °C and 900 °C.

The presence of the strong Me-C peak, together with the results of the XRD analysis, suggests that a random solid solution structure was obtained. However, the presence of very small amounts of carbides, especially in the column boundaries, cannot be ruled out. Therefore, further TEM analysis was necessary to investigate possible carbides at the column boundaries further. The intensity, the shape and the peak position of Me-C peak and stay roughly the same, indicating that no carbon segregation into an amorphous carbon tissue phase, occurred. The amount of free carbon (C-C peak) is decreasing, as a function of the annealing temperature which indicates that free carbon may go into solid solution or forming a carbide phase. It is, however, important to note that the C-C peaks are due to their low intensity in the signal range of the background noise. This can be best observed in the spectra shown in Figure 17(a). Peak fitting is therefore rather difficult and inaccurate. No reliable quantification of the free carbon was obtained from the acquired XPS spectra. However, APT analysis carried out at Jochen Schneiders group at RWTH Aachen, which has been done outside the scope of this work, estimated that only a very small amount of carbon is present in carbon clusters. Furthermore, the APT analysis strongly supported that no carbides were present, and in fact, a solid solution structure was obtained [9].

Bright field STEM cross section overviews of the TaW and TaW(C) films, both in the as-deposited state and after annealing, are shown in Figure 18. The TaW films exhibited a thickness of ~ 500 nm, whereas the TaW(C) films exhibited a thickness of ~ 625 nm. A decidedly columnar structure extending over the entire film from the substrate surface to the top was observed for all investigated films. When comparing the columnar grains there is a distinct difference between the TaW and the TaW(C) films. The grains of the TaW films, depicted in Figure 18(c), seem to grow in a cone-like structure, very narrow at the bottom, near the film/substrate interface, and broad at the top of the films. The TaW(C) films, however, display a constant column width throughout the whole film as highlighted in Figure 18(d). This could be a result of the continuous renucleation during grain growth, caused by the addition of carbon. Hence the microstructure of the TaW(C) films is more polycrystalline with finer grains. The grains of the TaW(C) films exhibit a column width of about 15 ± 5 nm, compared with a width of 20 ± 5nm for the TaW films. Considering the rather large margin of error, the results are in agreement with the grain width found in the SEM top view analysis. No change of the column width was observed comparing the as-deposited and annealed state of the films, hinting that no grain coarsening occurred. However, the determination of the column width is not very representative, because of the low statistical accuracy since only a few columnar grains of the whole sample are evaluated.

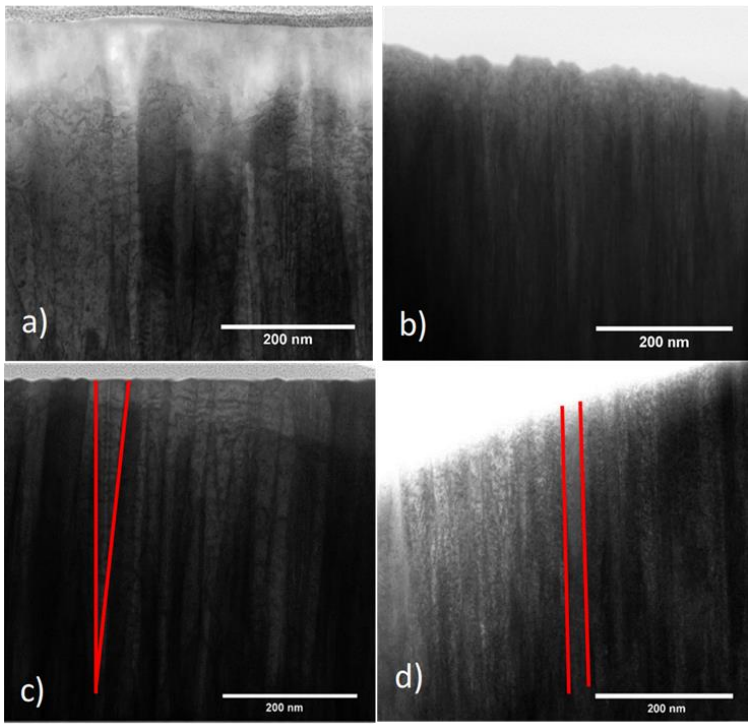

Figure 18: STEM bright field cross-section overview of a) TaW (~500nm) and b) TaW(C) (~625 nm) FIB lamella as-deposited, and c) TaW d) TaW(C) after annealing at 900 °C

A comparison of the surface morphology TaW and TaW(C) samples, in the as-deposited state and after annealing, is shown in Figure 19. The SEM images display a close resemblance in terms of structural features and their dimensions for Figure 19(b) and (d). The angular correlation of the surface morphology gives evidence of a strong orientation relationship between the grains of the films and is characteristic for all films. To estimate the grain size, or more precisely the width of the needlelike grains, the linear intercept method was used. The grain width is around 20 ± 5 nm and the length is 150 ± 10 nm, both for the TaW and the TaW(C) films. No significant coarsening of the columns could be observed when comparing the as-deposited and the annealed state. The surface morphology in the SEM top view resembled the structure found by Fritze et al. for the TaW-rich HEA films [8]. They introduced an atomistic model extrapolated from the cross-section, including the crystallographic orientation of the grains, explaining the strong angular correlation.

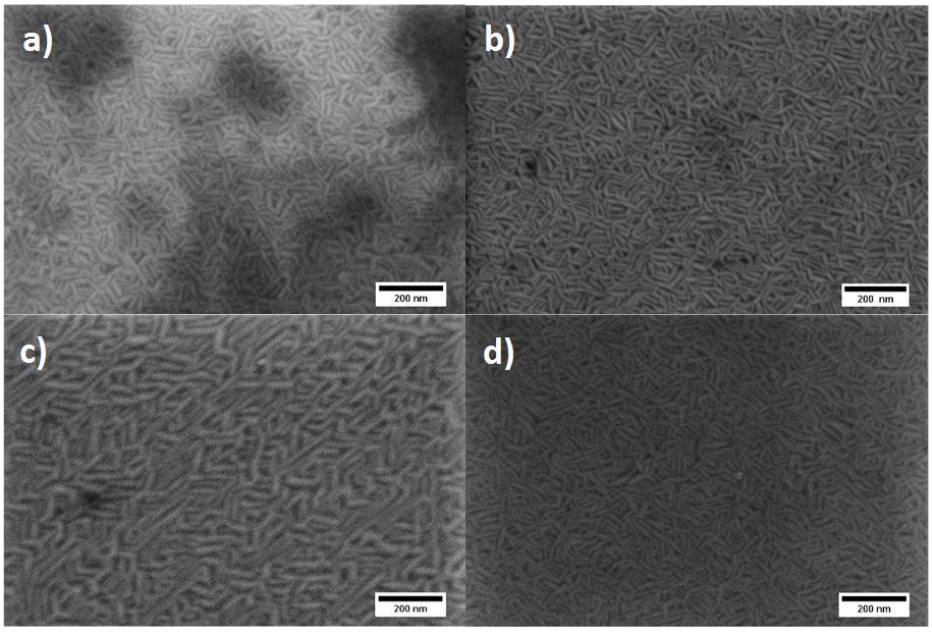

Figure 19: SEM top view images of a) TaW and b) TaW(C) as-deposited, c) TaW and d) TaW(C) both annealed at 900 °C

The STEM EDS underlines the elemental composition determined by APT [9], both for the TaW and TaW(C) samples, presented in Table 3. Elemental mapping showed an even distribution of both tantalum and tungsten in the as-deposited TaW film. However, the STEM EDX line scan presented in Figure 20 showed a slight enrichment of tungsten at the column boundary of the annealed TaW film. The investigated column boundary is marked in the STEM image and the W concentration is depicted by the red line diagram in the upper right of Figure 20. Schuh and Murdoch predicted a reversed trend when studying grain boundary segregation based on enthalpy calculations [52]. Further analysis is currently carried out to explain this effect.

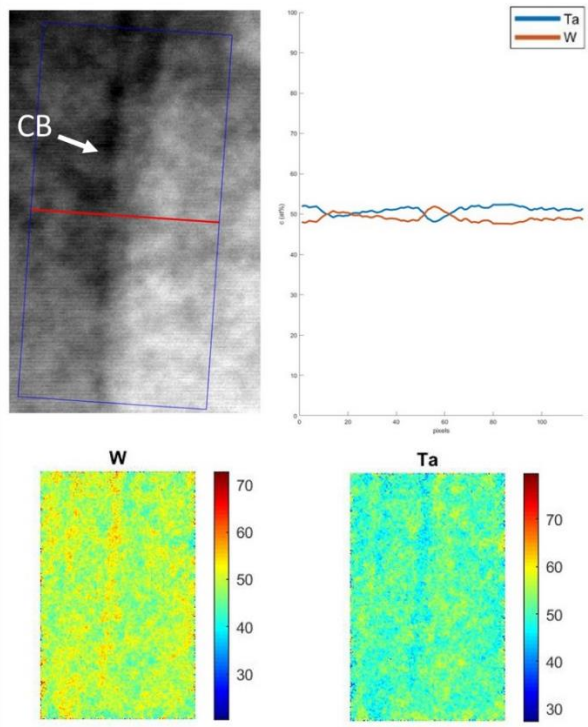

Figure 20: EDS line scan and elemental mapping of the TaW annealed at 900 °C

The TEM EDS analysis for the TaW(C) films are in agreement with the APT results and elemental mapping showed a random distribution of all three elements, confirming the proposed solid solution structure [9]. In Figure 21 the EDS elemental mapping of TaW(C) after annealing at 900 °C is shown. The investigated column boundary is marked in the HAADF image and contrary to the TaW films, no segregation of W was observed. Furthermore, no indications of carbide precipitates or carbon segregation could be found. This conclusion has also been underlined by recent APT results [9]. It is important to note though, that the determination of a light element like carbon is less accurate, especially with a low concentration like 6 at.% and in close proximity to heavy elements like Ta and W.

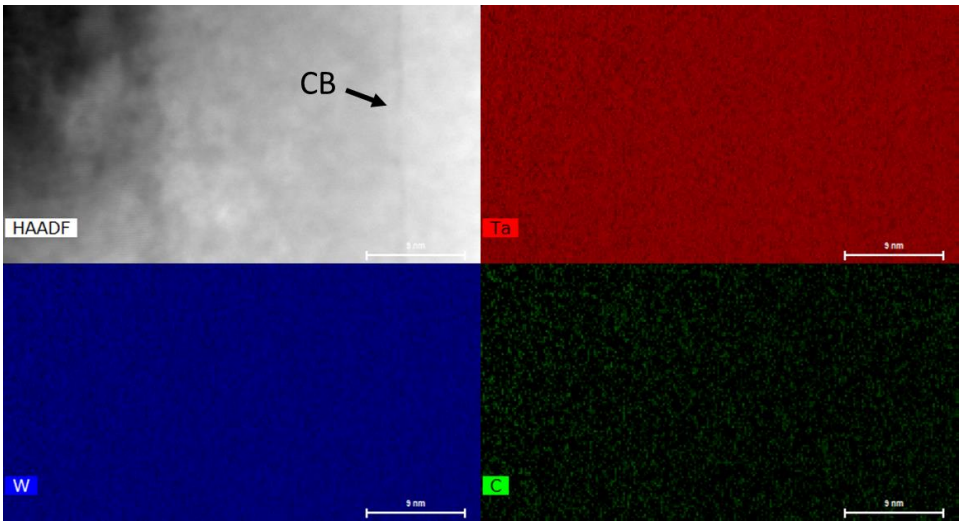

Figure 21: EDS elemental mapping of the TaW(C) annealed at 900 °C

In Figure 22 HR-STEM images of the corresponding lamellas depicted in Figure 18(a) and (c) are shown. The TaW films exhibit coherent grain boundaries, both in the as-deposited and in the annealed state. For the as-deposited TaW film, no atomic resolution could be obtained. The rows of atoms appear as lines because the lamella could not be prepared thin enough. The column boundary of the annealed TaW film in Figure 22(b) is highlighted in blue. There are no, or very few anti-phase boundaries in the examined sample area. However, there is a certain contrast between the two grains, due to a shift or rotation of the column against each other. The two grains have a different orientation, but it changes seamlessly at the grain boundary, which has been observed and discussed in detail by Fritze et al. [8].

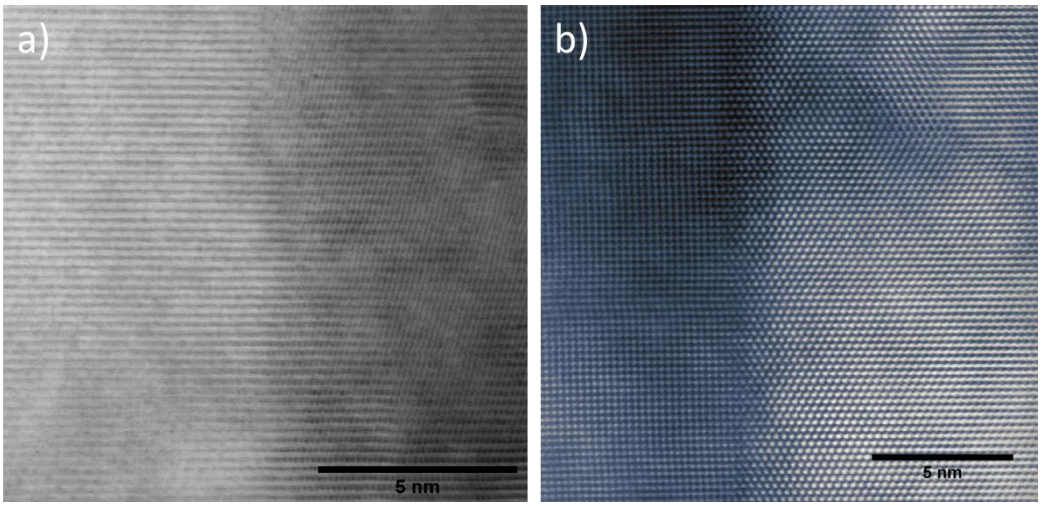

Figure 22: HR-STEM of one grain boundary of the a) as-deposited and b) annealed TaW sample. The magnification to the right illustrates the perfect column boundaries observed in TaW.

Compared with the metallic TaW film, the TaW(C) sample, corresponding to the lamella in Figure 18(d) appeared to have a more complex microstructure. In Figure 23 two areas are highlighted, showing anti-phase grain boundaries and dislocations. The observed anti-phase grain boundaries indirectly indicate an ordered structure. It is presumed that dislocation motion through an ordered – so-called superlattice – structure would lead to the formation of anti-phase grain boundaries. However, this ordering does not necessarily mean a change in the lattice structure, instead, it stems from the rearrangement of atoms on lattice sites [53,54].

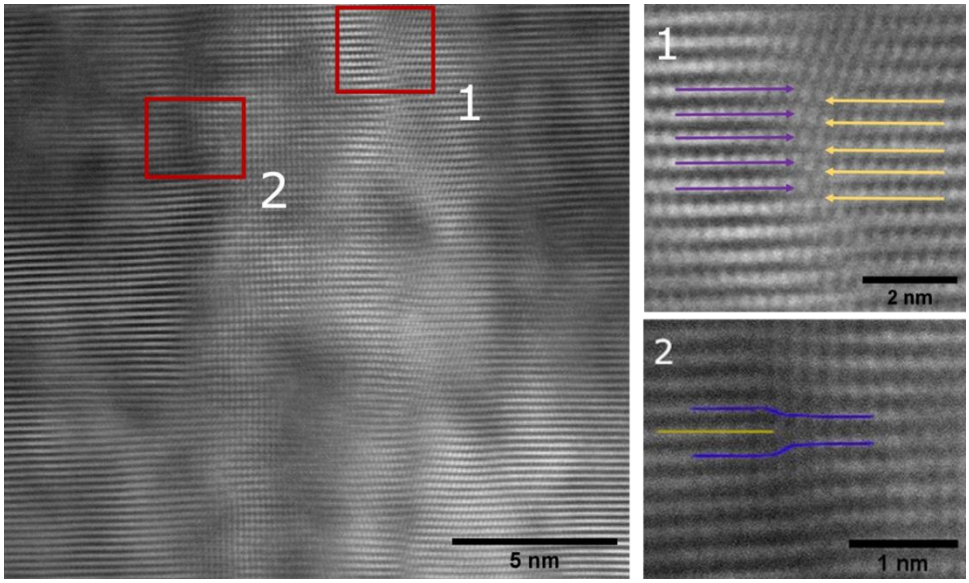

Figure 23: HR-STEM image of the annealed TaW(C) sample. 1) Anti-phase grain boundary and 2) Dislocation

In summary, the results above confirm that a supersaturated solid solution is formed, and that C remains in the solid solution structure after annealing at 900 °C for 2 hours. This observation suggests that the cell parameter reduction in Figure 15, where the cell parameter of the annealed TaW(C) film decreased to the value of the as-deposited TaW sample, is still unresolved. However, if the carbon was not pushed out of the structure, there must be a different explanation for the reduction of the unit cell such as strain relaxation or a significant atomistic reshuffling of the interstitial carbon.

Nanoindentation measurements were carried out on the TaW and TaW(C) films to evaluate the mechanical properties (hardness and reduced elastic modulus). The results for both the hardness H and the reduced elastic modulus E_r are presented in Figure 24. An increase in hardness after the heat treatment could be observed both for the metallic and the carbon supersaturated films, whilst the elastic modulus remained roughly the same in the range of 360-370 GPa. The hardness for the TaW and TaW(C) films in the as-deposited state was determined to be 12 and 16 GPa, respectively. Wang et al. have reported a similar hardness of 14.3 GPa for TaW thin films. Different factors such as stress, column size, composition and orientation, and possible superstructure formation can explain the minor difference in the hardness value compared to reference [55]. Furthermore, Wang et al. observed the formation of the β-TaW phase, which has a different cubic crystal structure and hence exhibits different mechanical properties. The highest hardness was observed for the samples after annealing at 900 °C with 17 GPa for TaW and 26 GPa for the TaW(C) films. These hardness values are in good agreement with previous studies by Palmquist et al. and Yang et al. [56].

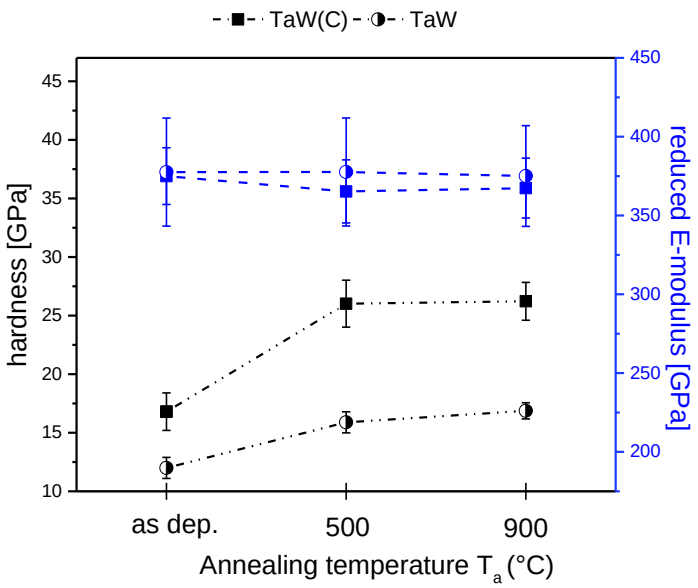

Figure 24: Hardness H and reduced elastic modulus E_r of the metallic TaW and carbon-containing TaW(C) films as a function of the annealing temperature T_a

The increased hardness of the TaW(C) film compared to the TaW film could be explained by the increasingly complex microstructure, as indicated by the TEM analysis. The dislocation movement is hindered by the more defective column boundaries and the carbon in interstitial sites. The TEM investigations also indicate that anti-phase boundaries have formed, which is proof of the formation of ordered structures (superstructures). The formation of such superstructures – enabled by the increased diffusivity at higher temperatures – can explain the

significant increase in hardness because ordered structures provide a higher lattice resistance. However, this seems to be more pronounced for the carbon-containing TaW films, indicates that the crucial point appears to be the distribution of the C interstitial. Further supporting that the ordering seems to be dominated by the C atoms is that the TaW(C) films exhibit nearly the same hardness after 500 or 900 °C, where only C presents sufficient diffusivity at 500 °C. But also, the fraction of C–C bonds within TaW(C) coatings decreases upon annealing, as seen in Figure 17, possibly leading to increased hardness as well.

Although significantly smaller, also the hardness of TaW films increases upon annealing. This smaller increase (as compared with the C-containing TaW film) supports the suggestion, that the hardness increase is driven by the formation of superstructures (which is less pronounced in the C-free film) and the reduction of weaker C–C bonds. Furthermore, slight segregation of W to the grain boundaries of the annealed TaW films was observed, which could influence the hardness. The reduction of the cell parameter for the annealed TaW(C) films, observed in Figure 15, suggests that upon annealing also the compressive stresses decrease. Since the supersaturated solid solution structure was retained, and no carbon precipitation occurred, typically the hardness should thus decrease. Therefore, the above-mentioned additional mechanisms (superstructure formation and reduction of weak C–C bonds) need to be the main reason for the increase in hardness

8. Conclusions

This thesis dealt with the topic of carbon supersaturation of refractory metal coatings, particularly Ta and W films. Investigating this very interesting concept and its limitations, the project can be separated into two main parts.

The first section focused on testing the limits of the carbon supersaturation concept within the W system. Films of W with a varying carbon concentration were deposited altering the power applied to the carbon target during deposition. The carbon concentration of the obtained films ranged between 0 and 10 at.%, resulting in a single solid solution phase with a bcc structure throughout the whole series. However, the mechanical properties, namely hardness and elastic modulus, displayed a peak performance around 9 at.% of carbon, declining with an increased amount of carbon dissolved in the structure.

The second part dealt with the investigation of the thermal stability of TaW(C) films. Based on the results obtained within the scope of this thesis, we can conclude that the solid solution structure was retained after the thermal treatment. A solid solution single phase bcc structure, with strong (110) texture was observed after annealing to 500 and 900 °C for two hours. Contrary to expectations, no indication of carbon precipitation was found. Neither carbide nor amorphous tissue phase were observed in any of the analyses carried out. However, it should be noted that small variations in the carbon content is difficult to observe with EDS. Other techniques, such as atomic probe tomography (APT) should, therefore, be used to more accurately determine C segregation in the annealed films. In fact, after finishing my experimental work in Uppsala, the annealed TaW-C film was analysed with APT in RWTH Aachen confirming that no carbides or column boundary segregation of C occurs at this temperature. However, a minor clustering of C was observed. Furthermore, no grain coarsening occurred. The annealing also led to a significant increase in hardness for the TaW(C) films with an unchanged elastic modulus. The increase in hardness can be explained by the increasingly complex microstructure after annealing, namely an ordered superlattice structure, as observed in the TEM analysis. However, further investigation into the structure and the bonding states of carbon are currently carried out, using EXAFS for example.

With both superior mechanical properties, as well as the good thermal stability of the inherently thermodynamically unfavourable structure, the concept of carbon supersaturation of refractory metal coatings can be considered interesting for various potential applications. However, further more elaborate tests of the mechanical and electrochemical properties, like crack and corrosion resistance, should be done. Especially for applications where pure W or even TaW alloy coatings might be too brittle, the carbon supersaturation concept could pave the way to strengthened but still ductile refractory metal thin films.

List of figures

Figure 1: Ternary phase diagram of the W-Ta-C system [12] 3
Figure 2: Schematic of a basic sputter process [17] 6
Figure 3: a) Volmer-Weber b) Frank van der Merwe and c) Stranski-Krastanov [24] 8
Figure 4: Structure Zone diagram by Anders [29] 9
Figure 5: Bragg condition for diffraction on lattice planes [34] 12
Figure 6: Bragg-Brentano diffraction [34] 12
Figure 7: a) XRD geometry b) dependency of the diffraction volume with the incoming angle θ [39] 13
Figure 8: Load-displacement curve [41,42] 14
Figure 9: Pear-shaped interaction volume 15
Figure 10: (a) θ2θ -XRD patterns of the W(C) films with varying carbon concentrations. The green triangles and dashed lines indicate the peaks of the bcc phase. (b) Their respective cell parameters. 20
Figure 11: GI-XRD patterns of the W(C) films with varying carbon concentrations 21
Figure 12: SEM top view of a) and b) pure W, c) and d) W(C) with 6 at.% of carbon 21
Figure 13: Hardness H and reduced elastic modulus Er of the W(C) films as a function of the carbon concentration 22
Figure 14: θ2θ-XRD patterns of the TaW films in the as-deposited state and after annealing at 500 °C and 900 °C. The green triangles and dashed lines indicate the peaks of the bcc phase. 24
Figure 15: a) θ2θ-XRD patterns of the TaW(C) films in the as-deposited state and after annealing at 500 °C and 900 °C and b) their respective cell parameters. 24
Figure 16: GIXRD patterns of a) TaW films and b) TaW(C) films as-deposited, annealed at 500 °C and 900 °C. The green triangles indicate the peaks of the bcc phase. 25
Figure 17: XPS C1s spectra of TaW(C) as-deposited, annealed at 500 °C and 900 °C. 26
Figure 18: STEM bright field cross-section overview of a) TaW (~500nm) and b) TaW(C) (~625 nm) FIB lamella as-deposited, and c) TaW d) TaW(C) after annealing at 900 °C 27
Figure 19: SEM top view images of a) TaW and b) TaW(C) as-deposited, c) TaW and d) TaW(C) both annealed at 900 °C 28
Figure 20: EDS line scan and elemental mapping of the TaW annealed at 900 °C 29

Figure 21: EDS elemental mapping of the TaW(C) annealed at 900 °C 30
Figure 22: HR-STEM of one grain boundary of the a) as-deposited and b) annealed TaW sample. The magnification to the right illustrates the perfect column boundaries observed in TaW. 30
Figure 23: HR-STEM image of the annealed TaW(C) sample. 1) Anti-phase grain boundary and 2) Dislocation 31
Figure 24: Hardness H and reduced elastic modulus E_r of the metallic TaW and carbon-containing TaW(C) films as a function of the annealing temperature T_a ... 32

List of tables

Table 1: Heating profile of the annealing step 18
Table 2: Chemical composition of the W(C) samples from ERDA..... 19
Table 3: Chemical composition of the TaW(C) samples from APT [9] and TEM EDS 23

List of abbreviations

HEA ..... high entropy alloy

bcc ..... base centred cubic

fcc ..... face centred cubic

PVD ..... physical vapor deposition

CVD ..... chemical vapor deposition

S ..... sputter yield

DC ..... direct currency

SZM ..... structure zone model

T_h ..... homologous temperature

UHV ..... ultra-high vacuum

ERDA ..... elastic recoil detection analysis

ToF-E ..... time of flight energy

XPS ..... X-ray photoelectron spectroscopy

E_b ..... Binding energy

E_k ..... Kinetic energy of photoelectron

Φ ..... work function

XRD ..... X-ray diffraction

GIXRD ..... grazing incidence x-ray diffraction

λ ..... wave length

FWHM ..... Full Width Half Maximum

SEM ..... scanning electron microscopy

BSE ..... back scattered electron

SE ..... secondary electron

EDS ..... energy dispersive spectroscopy

TEM ..... transmission electron microscopy

HRTEM ..... high resolution transmission electron microscopy

STEM ..... scanning transmission electron microscopy

NBD ..... nanobeam diffraction

APT ..... atomic probe tomography

h_{max} ..... maximum penetration depth

h_r ..... residual penetration depth

h_e ..... elastic penetration depth

h_c ..... depth of the contact circle

P_{max} ..... maximal load

H ..... hardness

E_r ..... reduced elastic modulus

T_a ..... annealing temperature

T_{sub} ..... substrate temperature

RT ..... room temperature

EXAFS ..... extended X-ray absorption fine structure

List of references

[1] J.W. Yeh, S.K. Chen, S.J. Lin, J.Y. Gan, T.S. Chin, T.T. Shun, C.H. Tsau, S.Y. Chang, Nanostructured high-entropy alloys with multiple principal elements: Novel alloy design concepts and outcomes, *Adv. Eng. Mater.* **6** (2004) 299–303. doi:10.1002/adem.200300567.

[2] B. Cantor, I.T.H. Chang, P. Knight, A.J.B. Vincent, Microstructural development in equiatomic multicomponent alloys, *Mater. Sci. Eng. A.* **375–377** (2004) 213–218. doi:10.1016/j.msea.2003.10.257.

[3] J.W. Yeh, Recent progress in high-entropy alloys, *Ann. Chim. Sci. Des Mater.* **31** (2006) 633–648.

[4] R. Kozak, A. Sologubenko, W. Steurer, *Single-phase high-entropy alloys – an overview*, 230 (2015) 55–68. doi:10.1515/zkri-2014-1739.

[5] Z. Li, C.C. Tasan, H. Springer, B. Gault, D. Raabe, Interstitial atoms enable joint twinning and transformation induced plasticity in strong and ductile high-entropy alloys, *Sci. Rep.* **7** (2017) 1–7. doi:10.1038/srep40704.

[6] P.H. Mayrhofer, C. Mitterer, L. Hultman, H. Clemens, Microstructural design of hard coatings, *Prog. Mater. Sci.* **51** (2006) 1032–1114. doi:10.1016/j.pmatsci.2006.02.002.

[7] J. Bok, J. Wung, Z. Li, J. Chan, J. Gi, D. Raabe, H. Seop, Acta Materialia Boron doped ultrastrong and ductile high-entropy alloys, *Acta Mater.* **151** (2018) 366–376. doi:10.1016/j.actamat.2018.04.004.

[8] S. Fritze, P. Malinovskis, L. Riekehr, L. von Fieandt, E. Lewin, U. Jansson, Hard and crack resistant carbon supersaturated refractory nanostructured multicomponent coatings, *Sci. Rep.* **8** (2018) 1–8. doi:10.1038/s41598-018-32932-y.

[9] S. Fritze, M. Hans, B. Osinger, L. Riekehr, J.M. Schneider, U. Jansson, On the thermal stability of nanostructured carbon supersaturated refractory coatings, Manuscr. (n.d.).

[10] D.A. Vaughan, O.M. Stewart, C.M. Schwarty, Determination of interstitial solid-solubility limit in tantalum and identification of the precipitiate phases, *UC-25 Metall. Ceram.* (1960) 399–404.

[11] H.J. Goldschmidt, J.A. Brand, The tungsten-rich region of the system tungsten-carbon, *J. Less Common Met.* **5** (1963) 181–194.

[12] E. Rudy, *Ternary Phase Equilibria in TM-B-C-Si-Compendium of Phase Diagram Data*, 1969.

[13] M. Ohring, *The Material Science of Thin Films*, 2001.

[14] X. Feng, J. Zhang, Z. Xia, W. Fu, K. Wu, G. Liu, J. Sun, Stable nanocrystalline NbMoTaW high entropy alloy thin films with excellent mechanical and electrical properties, *Mater. Lett.* **210** (2018) 84–87. doi:10.1016/j.matlet.2017.08.129.

[15] D. Mattox, *Handbook of Physical Vapor Deposition (PVD) Processing*, 2010.

[16] P. Mayrhofer, *Surface Technology*, 2016.

[17] W.D. Westwood, *Sputter Deposition*, 2003.

[18] K. Wasa, *Handbook of Sputter Deposition Technology*, 2012.

[19] S. Haschmi, *Comprehensive Materials Processing*, 2014.

[20] K. Wasa, M. Kitabatake, H. Adachi, *Thin Film Materials Technology: Sputtering of Compound Materials*, William Andrew, 2004.

[21] F.C. Frank, J.H. van der Merwe, One-dimensional dislocations. II. Misfitting monolayers and oriented overgrowth, *Proc. R. Soc. London. Ser. A*, **19** (1949) 216.

[22] M. Volmer, A. Weber, Keimbildung in übersättigten Gebilden, *Zeitschrift Für Phys. Chemie.* **119** (1926) 277.

[23] I.N. Stranski, L. Krastanov, Theorie der orientierten Ausscheidung von Ionkristallen aufeinander, Sitzungsber. *Akad. Wiss. Wien, Math.-Naturwiss. Kl. IIb.* **146** (1928) 797.

[24] T. Grzela, Comparative STM-based study of thermal evolution of Co and Ni germanide nanostructures on Ge (001), (2015).

[25] E. Bauer, Phänomenologische der Kristallabscheidung an Oberflächen. I., *Zeitschrift Für Krist.* **110** (1958) 372.

[26] I. Petrov, P.B. Barna, L. Hultman, J.E. Greene, Microstructural evolution during film growth, *J. Vac. Sci. Technol. A Vacuum, Surfaces, Film.* **21** (2003) S117–S128. doi:10.1116/1.1601610.

[27] B.A. Movchan, A. Demchishin, V, *Phys. Met. Met.* **28** (1969) 83.
[28] J.A. Thornton, The microstructure of sputter-deposited coatings, *J. Vac. Sci. Technol. A Vacuum, Surfaces, Film.* **4** (1986) 3059–3065. doi:10.1116/1.573628.
[29] A. Anders, A structure zone diagram including plasma-based deposition and ion etching, *Thin Solid Films.* **518** (2010) 4087–4090. doi:10.1016/j.tsf.2009.10.145.
[30] S. Hüfner, *Photoelectron Spectroscopy*, Springer Berlin Heidelberg, 1996. doi:10.1007/978-3-662-03209-1.
[31] W. Assmann, H. Huber, S. Ch., M. Dobler, H. Glückler, A. Weidinger, Elastic recoil detection analysis with heavy ions, *Nucl. Instruments Methods Phys. Res. Sect. B Beam Interact. with Mater. Atoms. B* **131-136** (1994). doi:10.1016/S0168-583X(97)00872-0.
[32] B. Schmidt, K. Wetzig, *Ion Beams in Material Processing and Analysis*, Springer Science and Business Media, 2012.
[33] J. Epp, *X-Ray Diffraction (XRD) Techniques for Materials Characterization*, Elsevier Ltd, 2016. doi:10.1016/B978-0-08-100040-3.00004-3.
[34] L. Spieß, G. Teichert, R. Schwarzer, H. Behnken, C. Genzel, *Moderne Röntgenbeugung*, Vieweg+Teubner, Wiesbaden, 2009. doi:10.1007/978-3-8349-9434-9.
[35] R.E. Dinnebier, S.J.L. Billinge, Overview and Principles of Powder Diffraction, *Int. Tables Crystallogr.* **H** (2014) 1–19.
[36] S. Schorr, C. Stephan, T. Törndahl, Mainz;Roland, X-Ray and Neutron Diffraction on Materials for Thin-Film Solar Cells, in: *Adv. Charact. Tech. Thin Film Sol. Cells*, Wiley-VCH Verlag, 2011: pp. 347–363.
[37] S.L. Chang, Thin-film characterization by grazing incidence X-ray diffraction and multiple beam interference, *J. Phys. Chem. Solids.* **62** (2001) 1765–1775. doi:10.1016/S0022-3697(01)00109-3.
[38] R.L. Kautz, Reports on Progress in Physics Related content, *Rep. Prog. Phys.* (1996). doi:10.1088/0034-4885/77/5/056502.
[39] N. Nedfors, Synthesis and Characterization of Multifunctional Carbide- and Boride-based Thin Films, Acta Universitatis Upsaliensis, 2014.
[40] W.C. Oliver, G.M. Pharr, An improved technique for determining hardness and elastic modulus (Young's modulus), (2014). http://journals.cambridge.org.
[41] A.C. Fischer-Cripps, Nanoindentation, (2011) 21–38. doi:10.1007/978-1-4419-9872-9.
[42] W.C.C. Oliver, G.M.M. Pharr, Improved technique for determining hardness and elastic modulus using load and displacement sensing indentation experiments, *J. Mater. Res.* **7** (1992) 1564–1580. doi:10.1557/JMR.1992.1564.
[43] J.J. Friel, *X-ray and image analysis in electron microscopy*, 2nd ed., Princeton Gamma_Tech, 2003.
[44] R.. Egerton, *Physical principles of electron microscopy*, 2005. doi:10.3934/dcds.2018221.
[45] S.J. Pennycook, D.E. Jesson, High-resolution incoherent imaging of crystals, *Phys. Rev. Lett.* **64** (1990) 938–941. doi:10.1103/PhysRevLett.64.938.
[46] J.A. Panitz, The 10 cm atom probe, *Rev. Sci. Instrum.* **44** (1973) 1034–1038. doi:10.1063/1.1686295.
[47] J.A. Panitz, Imaging atom-probe mass spectroscopy, *Prog. Surf. Sci.* **8** (1978) 219–262. doi:10.1016/0079-6816(78)90002-3.
[48] Y. Suchorski, W. Drachsel, Fiel Ion Microscopy(FIM) and Atom Probe (AP), in: G. Friedbacher, H. Bubert (Eds.), *Surf. Thin Film Anal.*, 2nd ed., Wiley-VCH, 2011: pp. 237–257. doi:10.1007/s40279-013-0062-9.
[49] I. Djerdj, A.M. Tonejc, A. Tonejc, N. Radić, XRD line profile analysis of tungsten thin films, *Vacuum.* **80** (2005) 151–158. doi:10.1016/j.vacuum.2005.08.017.
[50] J.P. Palmquist, Z. Czigany, M. Odén, J. Neidhart, L. Hultman, U. Jansson, Magnetron sputtered W-C films with C60as carbon source, *Thin Solid Films.* **444** (2003) 29–37. doi:10.1016/S0040-6090(03)00937-4.
[51] Y. Pauleau, P. Gouy-Pailler, S. Païdassi, Structure and mechanical properties of hard W–C coatings deposited by reactive magnetron sputtering, in: *Metall. Coatings Thin Film.*, 1992: pp. 324–328.
[52] H.A. Murdoch, C.A. Schuh, Estimation of grain boundary segregation enthalpy and its role in

stable nanocrystalline alloy design, *J. Mater. Res.* **28** (2013) 2154–2163. doi:10.1557/jmr.2013.211.
[53] N.S. Stoloff, Ordered Alloys for High Temperature Applications, *MRS Proc.* **39** (1984). doi:10.1557/proc-39-3.
[54] M.. Marcinkowski, Treatise on Materials Science and Technology, in: H. Herman (Ed.), *Treatise Mater. Sci. Technol.*, Academic Press, New York, 1974.
[55] C.L. Wang, M. Zhang, J.P. Chu, T.G. Nieh, Structures and nanoindentation properties of nanocrystalline and amorphous Ta-W thin films, *Scr. Mater.* **58** (2008) 195–198. doi:10.1016/j.scriptamat.2007.09.042.
[56] L. Yang, C. Liu, M. Wen, X. Dai, Y. Zhang, X. Chen, K. Zhang, Small atoms as reinforced agent for both hardness and toughness of Group-VIB transition metal films, *J. Alloys Compd.* **735** (2018) 1105–1110. doi:10.1016/j.jallcom.2017.11.208.